Possible signals in differentiating the quantum radiation reaction from the classical one

X. B. Li,[1] B. Qiao,[1,2,3,*] Y. L. Liao,[4] J. Wang,[1] L. F. Gan,[1] C. T. Zhou,[1,3] S. P. Zhu,[5,6] and X. T. He[1,2,5]

[1]*School of Physics, Center for Applied Physics and Technology, HEDPS, and SKLNPT, Peking University, Beijing 100871, China*

[2]*Collaborative Innovation Center of IFSA, Shanghai Jiao Tong University, Shanghai 200240, China*

[3]*Center for Advanced Material Diagnostic Technology, Shenzhen Technology University, Shenzhen 518118, China*

[4]*School of Physics and Materials Science, Anhui University, Hefei 230039, China*

[5]*Institute of Applied Physics and Computational Mathematics, Beijing 100094, China*

[6]*Graduate School of China Academy of Engineering Physics, P.O. Box 2101, Beijing 100088, China*

(Received 25 August 2019; revised manuscript received 19 February 2020; accepted 19 February 2020; published 16 March 2020)

A configuration to identify the stochastic effect of the quantum radiation reaction is proposed, where electrons are put in a standing wave of two colliding ultraintense lasers. By comparing the simulation results of the semiclassical and quantum models, we find that if the semiclassical model is used, a particular trapping of electrons between two electric-field nodes is induced, which, however, does not exist once the correct quantum model is applied. This results in different features of the electron density, energy, and angular distributions, which can be measured in experiments.

DOI: 10.1103/PhysRevA.101.032108

I. INTRODUCTION

An accelerating charge emits radiation, which in turn delivers an effective force on the radiating charge. As we know, in a self-consistent description of the motion of a relativistic electron in external electromagnetic fields, the radiation reaction (RR) must be taken into account. In fact, a detailed characterization of the RR is indispensable for a correct description of high-field experiments using the present multi-PW and next generation of 10-PW laser facilities, such as the Extreme Light Infrastructure [1], Apollon [2], Vulcan [3], and XCELS [4], with peak intensities 10^{22}–10^{24} W/cm^2. Although the RR plays more and more important roles in the dynamics of electrons and even ions within the interaction of an ultraintense laser and matter, the general self-consistent description of the RR is still a challenging problem in classical and quantum electrodynamics (QED) [5].

The radiation reaction in the realm of classical electrodynamics, known as the classical radiation reaction, is well described by the Landau-Lifshitz (LL) equation when the quantum nonlinear parameter $\chi_e \equiv |e|\hbar\sqrt{(F_{\mu\nu}p^\nu)^2}/m^3c^4 \ll 1$, where $F_{\mu\nu}$ is the electromagnetic field tensor, $p^\nu = (\epsilon/c, \boldsymbol{p})$ is the electron four-momentum, γ is the Lorentz factor, $e < 0$ and m are the charge and mass of an electron, respectively, and c is the velocity of light. When χ_e approaches unity, the LL equation may no longer be assumed valid because the discrete nature of the photon emission cannot be neglected in the dynamics of the electron. Hence, the motion of an electron with the RR in this regime should be described within the framework of QED, which is known as the quantum regime of the radiation reaction. In order to find evidence of the quantum RR, experiments have recently been conducted using a high-energy electron beam generated by a laser wakefield accelerator colliding head-on with an ultraintense laser. The postcollisional electron spectra are computed by using semiclassical and quantum models and compared with the experimental results [6,7].

The semiclassical model is based on the classical LL equation which is modified by introducing a quantum correction. As we know, the unphysical emission of a photon with an energy higher than the initial kinetic energy of the emitting electron is allowed in the classical theory, which leads to overestimation of the electron energy loss [8]. Nevertheless, this can be settled by limiting the highest radiated frequency from the viewpoint of quantum theory, which has been thoroughly investigated in the literature [8–12].

The quantum RR is taken into account by calculating the recoil of multiple incoherent single-photon emissions, which has been shown to contribute dominantly to the RR in the so-called moderate quantum regime [8]. This regime is defined by (i) the classical nonlinear parameter $a_0 = |e|E_0/m\omega_0 c \gg 1$, where E_0 is the laser electric-field amplitude and ω_0 is the central angular frequency, and (ii) the quantum nonlinear parameter $\chi_e < 1$. These two conditions ensure that the nonlinear QED effects are already important in this regime, while the electron-positron pair production is still negligible. In such a regime, the RR may reveal stochasticity because the emission of photons by an electron is substantially probabilistic. Actually, identifying the quantum nature of the RR is the main drive for the recent experiments mentioned above.

There have been numerous studies dedicated to identifying the signature of the quantum RR [10,12–22]. Almost all of these studies can be summarized in two aspects: The quantum RR predicts a reduction in radiation power and the quantum radiation has a stochastic nature. Most of previous works have focused on the first signature, yet uncertainties about

*Author to whom all correspondence should be addressed: bqiao@pku.edu.cn

the second signature of the quantum RR still remain [23]. Furthermore, works on the stochasticity of the quantum RR have mainly focused on the electron-beam spreading in the all-optical laser–electron-beam collision setup. This character of the quantum RR would narrow the radiation angle [24] and smooth the angular distribution of radiation generated by electrons [25]. However, it is worth noting that all of these schemes require not only the production of a high-quality high-energy electron beam but also its precise spatiotemporal alignment with the laser, which is quite challenging in experiments [18,26]. In addition, these findings are based on indirect measurement of postcollisional beam spreading or radiation distribution which are inevitably accompanied by large uncertainties. Thus, a direct and clear method for the identification of the quantum RR is still in need.

In this article we propose a configuration that uses relativistically transparent plasmas in a standing wave formed by two counterpropagating ultraintense lasers to identify the stochastic effect of the quantum radiation reaction on electrons. We find that if the semiclassical model is used, a particular trapping of plasma electrons between two electric-field nodes is induced, where electrons perform complex periodic motions between adjacent electric nodes of the standing wave and extra spikes of the electron density distribution form. However, this phenomenon does not exist once the correct quantum model is applied due to the stochasticity effect in the radiation reaction. The resultant different features in the electron density, energy, and angular distributions from two-dimensional particle-in-cell (PIC) simulations between two models have been analyzed in details and can be regarded as signals in differentiating the quantum radiation reaction from the classical one in experiments.

The paper is organized as follows. In Sec. II we briefly introduce the semiclassical and QED models we employ to study the dynamics of electrons in an ultraintense standing-wave field. In Sec. III we demonstrate the special characters of spatial, angular, and energy distributions induced by the quantum RR. In Sec. IV we discuss the impacts of various parameters of the laser and the target on the distribution of the electrons. We summarize in Sec. V.

II. RADIATION REACTION MODELS: FROM CLASSICAL THEORY TO QED

Before analyzing the dynamics of electrons in the ultraintense standing-wave field, we introduce the two RR models that will be used. The first model is a semiclassical model which is actually a modified Landau-Lifshitz (MLL) model, i.e., the classical LL equation with the overestimation of energy loss compensated by a function derived from quantum mechanics, namely, the Gaunt factor $g(\chi_e)$ [9,27]. The second one is a quantum stochastic model which is now widely included in QED PIC codes. The major difference between these two models is that the movements of electrons in the QED model possess the intrinsic stochastic nature induced by the stochastic emissions of photons.

In classical electrodynamics, it is known that the earliest attempt at a self-consistent solution for the coupled Maxwell-Lorentz equation led to the Lorentz-Abraham-Dirac (LAD) equation plagued by the unphysical self-acceleration solution. Then Landau and Lifshitz derived an equation, i.e., the celebrated LL equation [28], from the LAD equation by use of the iterative approach. This equation successfully eliminates the unphysical solution of LAD equation and keeps all the physical solutions, which can be written as follows:

$$\dot{p}_\mu = \frac{e}{m}F_{\mu\nu}p^\nu + \frac{2\alpha}{3}\left[\frac{e}{m^3}(\partial_\lambda F_{\mu\nu})p^\lambda p^\nu - \frac{e^2}{m^3}F_{\mu\nu}F^{\lambda\nu}p_\lambda + \frac{e^2}{m^5}F^{\sigma\nu}p_\nu F_{\sigma\lambda}p^\lambda p_\nu\right]. \tag{1}$$

Since classical electrodynamics allows unphysical emissions of photons with energy higher than that of the radiating electron, we have to manually reduce the radiation power by introducing the Gaunt factor [29], which is defined as [30–32]

$$g(\chi_e) = \frac{\int_0^{\chi_e/2} F(\chi_e, \chi_\gamma)d\chi_\gamma}{\int_0^\infty F_{cl}\left(\frac{4x}{3\chi_e^2}\right)d\chi_\gamma} = \frac{3\sqrt{3}}{2\pi\chi_e^2}\int_0^{\chi_e/2} F(\chi_e, \chi_\gamma)d\chi_\gamma, \tag{2}$$

where F_{cl} and F are the classical and quantum synchrotron functions, respectively. Usually, a good approximation of the Gaunt factor is used, which appears as [33]

$$g(\chi_e) \approx \left[1 + 4.8(1+\chi_e)\ln(1+1.7\chi_e) + 2.44\chi_e^2\right]^{-2/3}. \tag{3}$$

The balance condition between the Lorentz force and the RR force is crucial in electron dynamics, which we now try to estimate. For simplicity, we use normalized variables $t' = \omega t$, $\mathbf{x}' = k\mathbf{x}$, $\mathbf{v}' = \mathbf{v}/c$, and $(\mathbf{E}', \mathbf{B}') = e(\mathbf{E}, \mathbf{B})/m\omega c$, where $\omega = kc$ and k are the wave frequency and wave number, respectively. The spatial components of the semiclassical equation are then

$$\mathbf{f} = \mathbf{f}_L + g(\chi_e)\mathbf{f}_{RR} = (\mathbf{E} + \mathbf{v}\times\mathbf{B}) + g(\chi_e)\rho_f(\mathbf{f}_1 + \mathbf{f}_2 + \mathbf{f}_3), \tag{4}$$

where $\mathbf{E}$ and $\mathbf{B}$ are the external electric and magnetic field, respectively, $\rho_f = 2r_e k/3 \ll 1$, $r_e = e^2/mc^2$ is the classical electron radius, and

$$\mathbf{f}_1 = -\gamma^2[(\mathbf{E} + \mathbf{v}\times\mathbf{B})^2 - (\mathbf{v}\cdot\mathbf{E})^2]\mathbf{v}, \tag{5}$$

$$\mathbf{f}_2 = \gamma[(\partial_t + \mathbf{v}\cdot\nabla)\mathbf{E} + \mathbf{v}\times(\partial_t + \mathbf{v}\cdot\nabla)\mathbf{B}], \tag{6}$$

$$\mathbf{f}_3 = [\mathbf{E}\times\mathbf{B} + \mathbf{B}\times(\mathbf{B}\times\mathbf{v}) + \mathbf{E}(\mathbf{v}\cdot\mathbf{E})], \tag{7}$$

where γ is the Lorentz factor. The second term of the RR force $\mathbf{f}_2$ is the so-called Schott term, which can be neglected provided the field changes slowly with respect to the space and time. In the case of laser fields, the condition is $a_0\gamma \gg 1$ [34], which is already satisfied for the case considered in this article. At the ultrarelativistic limit $\gamma \gg 1$, $\mathbf{f}_3$ can be neglected since $\mathbf{f}_1$ is proportional to γ^2.

Assuming that $\gamma \approx a_0$ and $g(\chi_e) \sim 1$ for modest quantum effects, we find the amplitude of the first term in the RR force $f_1 \sim a_0^4$ [35]. Therefore, the balance condition between the RR and Lorentz forces can be roughly estimated as

$$a_0^3\rho_f \sim 1. \tag{8}$$

Note that it has been shown by Refs. [36,37] that at $a_0^3\rho \sim 1$, i.e., when the radiation reaction dominates, the electron motion in an ultraintense standing wave evolves to limit cycles, strange attractors, Lévy flights, and random walk. For a laser with a wavelength $\lambda = 2\pi/k = 1\ \mu$m, it yields

$$a_0 \approx \left(\frac{1}{\rho_f}\right)^{1/3} \approx 440. \tag{9}$$

In the quantum stochastic model, we employ a by-now-standard Monte Carlo method to calculate the emission of photons and the corresponding recoils. The stochastic emission of high-energy photons by an electron is considered by sampling synchrotron emission rate obtained from the strong-field QED theory. An electron stochastically emits high-energy photons through a sampling synchrotron emission rate obtained by strong-field QED theory. The RR effect is then taken into account following the conservation of momentum. Between these emission events, the electron dynamics in the external laser field is described by the Lorentz equation.

The rate of synchrotron emission is [27]

$$\frac{dN_\gamma}{dt} = \frac{\sqrt{3}\alpha_f c}{\lambda_c}\frac{\chi_e}{\gamma}\int_0^{\chi_e/2}\frac{F(\chi_e,\chi_\gamma)}{\chi_\gamma}d\chi_\gamma. \tag{10}$$

By sampling the emission rate using a Monte Carlo method, the electron emits a photon when the condition $\int_0^t dN_\gamma/dt\,dt' > \ln(1/P)$ is fulfilled, where P is chosen randomly in the interval [0, 1]. Apparently, such discontinuous emissions introduce a stochastic term into the equation of motion, which makes the electrons deviate from the deterministic trajectories predicted by the classical theory.

III. DISCERNING THE QUANTUM STOCHASTIC EFFECTS IN THE ELECTRON DISTRIBUTION

We begin by simulating the electron dynamics in the ultraintense standing wave of different amplitudes, utilizing the semiclassical model and the quantum model given above. The ultraintense standing wave is formed by two counterpropagating linearly polarized plane waves with the same wavelength $\lambda = 1\ \mu$m and the normalized intensity a_0 varying from 300 to 700. A thin layer of electron cloud with density $n_e = 0.001n_c$ is placed in the middle of the box. The simulations are carried out with the QED PIC code EPOCH [38]. For the quantum stochastic model, we employ the by-now-standard Monte Carlo method described in the preceding section (see Ref. [27] for details). For the semiclassical model, the complete form of the LL equation is implemented [Eq. (1)] into the particle pusher and benchmarked against Ref. [34] (see the Appendix for details). Then the Gaunt factor (3) is introduced to take into account the MLL model. The results obtained in Ref. [39] could also be reproduced with our code.

In Fig. 1 the long-term stable electron distribution is plotted as a function of the wave amplitude. The distribution is selected after 25 oscillations of the standing wave, when the distribution is already stabilized. It can be clearly seen that radiative trapping phenomena appear at electric-field nodes ($x = \pm\lambda/4$) when a_0 is above 300 [36,40–45]. The radiative trapping effect is well studied in the literature. The reason for this effect is that the magnetic field is always perpendicular to the velocity, while the electric field has parallel components. This leads to a higher radiation parameter χ_e at the maxima of the magnetic field, i.e., electric-field nodes. Electrons lose more energy at these locations and are consequently trapped. It is shown that the radiative trapping effect is not so significant for the quantum model since the trapped density is not so high as that of the MLL model. The reason is that the electrons are more likely to escape from the electric nodes due to the stochastic emission of photons. Thus the radiative trapping effect is weakened in the quantum model.

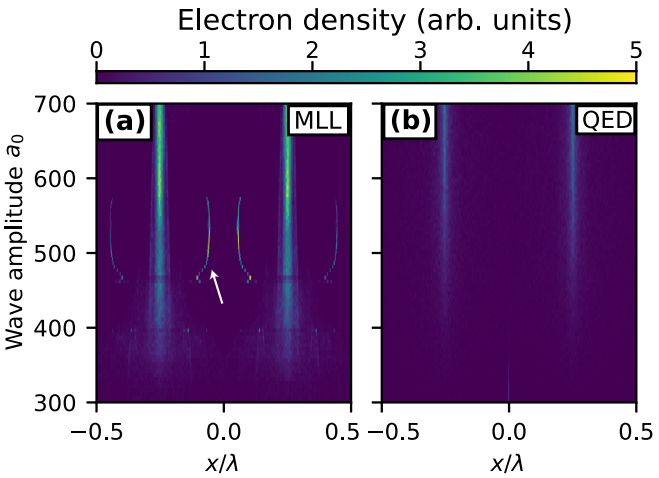

FIG. 1. Long-term density distribution of electrons in a standing wave as a function of wave amplitude a_0. (a) Modified Landau-Lifshitz model. Two extra density peaks are clearly seen with a_0 ranging from 460 to 560. (b) QED model. No attractors are shown.

Notably, in the semiclassical model, with a_0 around 500, electrons are not only trapped at the electric nodes, but also accumulated somewhere between two adjacent electric-field nodes [see the white arrow in Fig. 1(a)]. Hence two extra spikes emerge at the longitudinal electron distribution. In this setup, the Coulomb interaction between electrons is negligible because of the low density. The formation of such spikes is attributed to the balance between the RR force and Lorentz force, which indicates that a_0 should be around 440 according to the condition we obtained in Eq. (9). The estimation fits well with the simulation results.

Illustrated in Fig. 2 are the typical electron trajectories in the semiclassical model and the quantum model. We choose two electrons with exactly the same initial condition in the two models. In the semiclassical model, the electrons perform periodic motion following some deterministic trajectories. Actually, it was pointed out by Esirkepov and Bulanov [46] that a strong nonlinear highly oscillatory friction such as the RR leads to a paradoxical stabilization of the electrons near the electric nodes. In addition, this periodic motion is one type of limit cycle shown in Ref. [36]. Note that, despite continuous effort to develop analytical approaches [35,37,40,46,47], it is extremely difficult to obtain the exact analytical form of the trajectories due to the high degree of nonlinearity in the ultraintense standing wave. In the quantum model, however, as shown by the orange line in Fig. 2, electrons cannot sit on the periodic trajectories. Black circles in Fig. 2(a) denote the locations of photon emissions. It can be

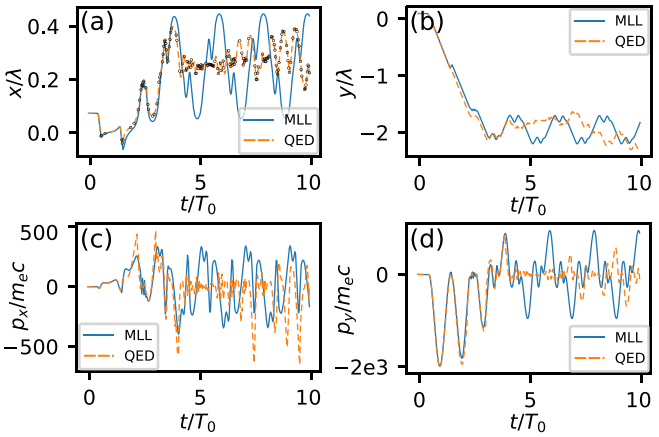

FIG. 2. Sampled electron trajectories: (a) x versus time, (b) y versus time, (c) p_x versus time, and (d) p_z versus time. We selected two electrons with the same initial condition. Solid blue lines represent the result from the MLL model, while dashed orange lines correspond to the result from the QED model. Black circles in (a) denote the location of photon emissions. In the MLL model, electrons perform periodic motion in an ultraintense standing wave, whereas in the QED model, electrons are trapped in the electric-field nodes.

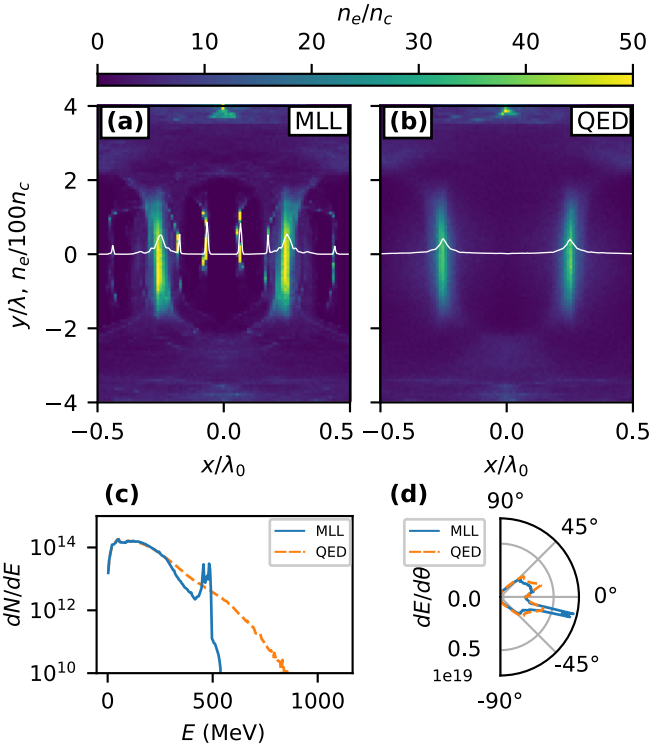

FIG. 3. (a) Electron density map at $15T_0$ in the realistic case in the MLL model. The white line depicts the longitudinal electron density distribution normalized by $100n_c$ at the same time. (b) Same as (a) but in the QED model. (c) Electron energy spectra recorded on a probe plane at $x = 3\lambda$. The solid blue line depicts results from the MLL model and the dashed orange line the QED model. (d) Corresponding electron energy angular distribution $dE/d\theta$, where $\theta = \arctan(p_y/p_x)$, recorded on the same probe plane.

seen that discontinuous photon emissions make the electron deviate from the periodic orbits and then fall into the electric nodes, which explains the absence of two extra spikes in the density distribution [see Fig. 1(b)].

To show that these findings can still hold in an actual experiment, we carry out a realistic setup by using the methods described above. Two counterpropagating linearly polarized ultraintense laser pulses, with the same wavelength $\lambda = 1\ \mu$m and amplitude $a_0 = 500$, are incident on an aluminum foil. Both lasers have the same spatiotemporal profile with duration $\tau = 10T_0$ and a focal radius of 2.5 μm. The temporal and spatial profiles are both fourth-order super-Gaussian. In the simulations, the simulation box is $[-5\lambda, 5\lambda] \times [-5\lambda, 5\lambda]$ discretized by 1000 cells along each axis. A fully ionized aluminum foil with electron density $n_e = 50n_c$, where n_c is the critical density 1.1×10^{21} cm^{-3} and the thickness $l_0 = 0.2\lambda$, is placed at the middle of the simulation box. Each foil cell is filled with 500 macroelectrons and 64 macroions. A probe plane is placed at $x = 3\lambda$, which records the electrons that traverse it. In this setup, the density of the aluminum target is lower than that of solids which may be realized, for instance, by using the metal foams or the sputtering techniques [44]. In addition, it is found that the result is insensitive to ion species.

The resulting electron density distribution is shown in Figs. 3(a) and 3(b). Even though we are using realistic parameters, the differences between the semiclassical model and the quantum model are still pronounced. The semiclassical theory predicts several density peaks resulting from the balance between the Lorentz force and RR force shown above, whereas the quantum model predicts no density peaks at all. This can be easily seen from the longitudinal density distributions of electrons which are displayed by the white lines. However, this feature does not exist in the quantum model. This exclusive feature of the classical radiation reaction could provide a method to distinguish a different radiation reaction model in a definitive way, rather than some quantitative differences such as average beam energy. Experimentally, the density distribution could be measured in principle by the interferometer and/or x-ray backlighting photography.

Moreover, the electron energy spectrum recorded on the probe plane is plotted in Fig. 3(c). Since electrons sitting on the periodic orbits are accelerated to very high energies [see Figs. 2(c) and 2(d)], the MLL model predicts a spectral peak in the electron energy spectrum at $E \approx 500$ MeV, whereas the QED model predicts no such peaks. Note that the cutoff energy of the QED model is higher than that of the MLL model, which is attributed to the straggling effect [48,49], indicating the broadening of the phase-space distribution [13,15]. Consequently, it is anticipated that the cutoff energy of the photon spectrum is also higher in the QED model than that in the MLL model. Meanwhile, Fig. 3(d) shows the angular energy distribution of electrons traversing the probe plane, where an evident peak is found at approximately -20° in the MLL model. In the experiment, the energy distribution can be obtained by placing a spectrometer on either side of the target, while the angular distribution can be measured by distributing detector arrays similar to that presented in Ref. [21].

The standing-wave structure is well formed at $10T_0$, as can be seen Figs. 4(a) and 4(b), where the left- and

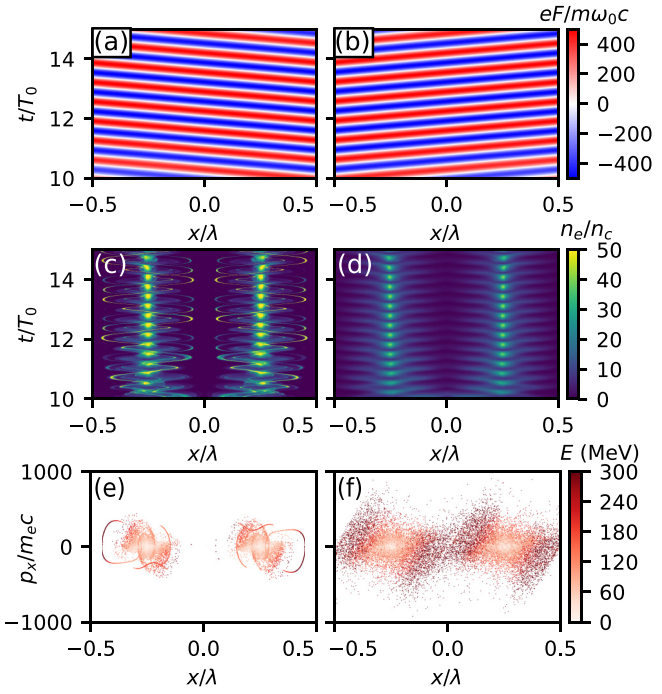

FIG. 4. (a) Spatiotemporal distribution of the left-propagating laser. (b) Same as (a) but for the right-propagating laser. (c) Longitudinal electron density evolution versus time for the MLL model. The density distribution is sampled at $y = 0$. (d) Same as (c) but for the QED model. (e) Poincaré section map showing 40 000 trajectories from $10T_0$ to $50T_0$ for the MLL model. Color denotes the electron kinetic energy. (f) Same as (e) but for the QED model with 30 000 trajectories.

right-propagating components of the standing wave versus time are shown. These components are defined as $F = (E_y \pm B_z)/2$, where $+$ denotes the right-propagating laser and $-$ denotes the left. It can be seen that lasers propagate through the plasma and remain unperturbed. The corresponding longitudinal electron density evolutions versus time are also plotted in the MLL model [Fig. 4(c)] and the QED model [Fig. 4(d)]. Also, a large number of electrons perform periodic oscillations near the electric nodes following the trajectories shown in Fig. 2. Such electrons form a density peak with a density 50 times higher than the critical density. However, the QED model reveals that no such additional density peaks would appear except those caused by the normal radiative trapping effect.

Figures 4(c) and 4(d) illustrate Poincaré section plots in the MLL model and the QED model, respectively. The longitudinal coordinate x and momentum p_x of an electron are recorded each time it traverses the $y = 0$ plane. The corresponding kinetic energies are denoted by colors. It can be seen that there are three attractors in $0 < x < 0.5\lambda$, corresponding to the three density peaks in Fig. 3. However, no such attractors are shown in the QED model and the electrons spread widely in the phase space due to the stochasticity effect.

To demonstrate that periodic orbits predicted by the MLL model do cause the energy peak at 500 MeV, the electron energy spectra recorded on a virtual detector for different laser amplitude a_0 are illustrated in Fig. 5. For parameters

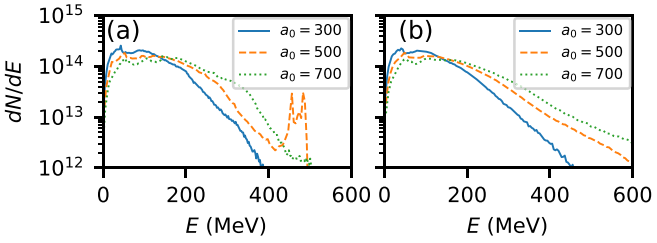

FIG. 5. Recorded electron energy spectra dN/dE on the virtual detector for different laser amplitude a_0 for (a) the modified LL model and (b) the QED model. The other parameters are the same as in Fig. 3.

not satisfying Eq. (9), i.e., $a_0 = 300$ or 700, there are no periodic orbits in the MLL model, as seen in Fig. 1. Hence, no signatures of any energy spikes are found in the energy spectra in the two cases [see the blue line and the green line in Fig. 5(a)].

IV. IMPACT OF LASER AND TARGET PARAMETERS

Now we investigate how the parameters of the laser and the target influence the electron distribution. We will address first the effect of the laser duration, then the importance of different target thickness, and finally the influence of the initial target density.

The results of an electron distribution with different values of the laser duration τ are shown in Figs. 6(a) and 6(d). When τ increases from $5T_0$ to $15T_0$, the spikes in the longitudinal density distribution of electrons are always there, indicating that the periodic motion of the electrons is maintained. One may be prompted to ask what the characteristic time is of these periodic orbital motions. In fact, the electrons fall rapidly into the periodic orbits in about three cycles of the laser, as shown in Fig. 2. The attraction timescale can be estimated as $\mathcal{T} \sim (\rho_f a^2 \gamma)^{-1}$ in units of the laser period T_0. Thus, the periodic orbital motions exist in the MLL model for various laser durations. On the contrary, only the normal attractors are present at the electric nodes when the QED model is employed to describe the motion of electrons, and no further density spikes emerge because the emission of photons is totally stochastic.

The effects of the target thickness on the spatial distribution of electrons are described in Figs. 6(b) and 6(e). As we know, the thickness of the target mainly affects the electrostatic pressure. If the target becomes thick enough, the charge separation field comes into play and disrupts the periodic trajectories of the electrons. Notice that the necessary condition for the formation of a stable standing wave is that the electrostatic pressure should be lower than the laser radiation pressure, i.e., $2\pi n_0^2 e^2 l_0^2 < I_0/c$, which means that the target should be as thin as possible. Otherwise, the hole-boring stage exists [45], hence distorting the standing wave. In the case considered here with $a_0 = 500$ and $n_e = 50n_c$, the thickness of the target should be thinner than $2\lambda_0$ to facilitate the formation of periodic orbits of electrons. However, when the QED model is applied, there are still no spikes in the distribution of electrons except the normal ones, no matter how thin the target is.

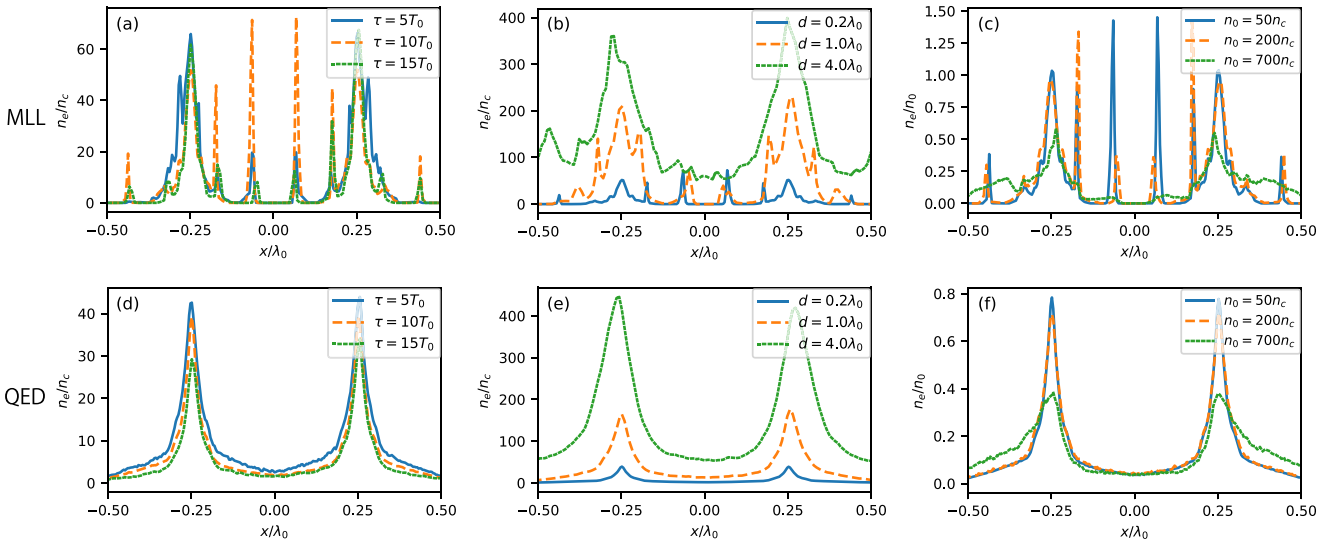

FIG. 6. Impacts of (a) and (d) laser duration, (b) and (e) target thickness, and (c) and (f) initial target density on the longitudinal electron density distribution at $15T_0$ for results obtained via (a)–(c) the MLL model and (d)–(f) the QED model. In (a) and (d) the solid blue (top), dashed orange (middle), and dotted green (bottom) curves represent the laser duration $\tau = 5T_0$, $10T_0$, and $15T_0$, respectively. In (b) and (e) the solid blue (top), dashed orange (middle), and dotted green (bottom) curves represent the target thickness $d = 0.2\lambda_0$, $1.0\lambda_0$, and $4\lambda_0$, respectively. In (c) and (f) the solid blue (top), dashed orange (middle), and dotted green (bottom) curves represent the target initial density $n_0 = 50n_c$, $200n_c$, and $700n_c$, respectively. The other laser and target parameters are the same as in Fig. 3.

Finally, the influence of the initial target density on the electron distribution is studied, as shown in Figs. 6(c) and 6(f). The ratio of the electron density n_e at $15T_0$ with respect to the initial density n_0 is plotted in different cases. Three values of the initial target density $50n_c$, $200n_c$, and $700n_c$ are considered here. We find that the periodic orbits and the particular trapping phenomenon apparently exist in the first two cases and disappear when $n_0 = 700n_c$. This can be explained from the following two aspects. On the one hand, in the case of $n_0 = 700n_c$, which is larger than the relativistic critical density $\gamma n_c \approx 500n_c$, the target is initially opaque to the laser. As a result, the standing wave forms at a much later time when the plasma temperature is significantly increased and the target becomes transparent due to thermal expansion, which suppresses the particular trapping effect in the MLL model above. On the other hand, similar to the case mentioned in Ref. [42], the maximum number of particles N inside this trapping is limited by their mutual Coulomb interaction, which can be estimated by equating the magnitude of the Lorentz force $F_L = eE$ to that of the Coulomb force at the edge of the trapping state $F_C = e^2N/4\pi\varepsilon_0 r^2$, with $r = 0.05\ \mu$m, as shown in Figs. 6(c) and 6(f). For the considered case here, $eE_{\max}/m\omega c = 2eE_L/m\omega c = 1000$, we obtain that $N = 3.0 \times 10^9$, which corresponds to the maximum density at the trapping center of $n_{\max} \approx 400n_c$, even smaller than the initial target density $n_0 = 700n_c$. This means that in the case of $n_0 = 700n_c$ the Lorentz force of the standing wave is not strong enough to overcome the Coulomb force and therefore the particular trapping phenomenon cannot occur even if the standing wave forms at a later time. Also note that the phase space in Fig. 4 shows significant heating and temperature increases, which may further inhibit the occurrence of the particular trapping between the standing-wave nodes due to an additional thermal pressure.

V. CONCLUSION

We have shown that the standing-wave configuration with a transparent plasma in two counterpropagating ultraintense lasers can be used to identify the stochastic effect of the quantum radiation reaction on electrons. We found that if the semiclassical model is used, a particular trapping of plasma electrons between two electric-field nodes is induced, where electrons perform complex periodic motions between adjacent electric nodes of the standing wave, and extra spikes of the electron density distribution form. However, this phenomenon does not exist once the correct quantum model is applied due to the stochasticity effect in the radiation reaction. This results in different features in the electron density, energy, and angular distributions between two models, which can be regarded as possible signals in verifying the QED model in experiments on current multi-PW or forthcoming 10-PW laser facilities.

ACKNOWLEDGMENTS

This work was supported by the Science Challenging Project No. TZ2018005, the NSAF Grant No. U1630246, the National Key Program of S&T Research and Development Grant No. 2016YFA0401100, and the National Natural Science Foundation of China Grants No. 11575298 and No. 11825502. B.Q. acknowledges support from National Natural Science Funds for Distinguished Young Scholar Grant No. 11825502.

APPENDIX: IMPLEMENTATION OF CLASSICAL RADIATION REACTION

The implementation of the classical RR is done by replacing the Lorentz equation of the particle pusher with the LL equation. The exact form (in SI units) that we used in our code

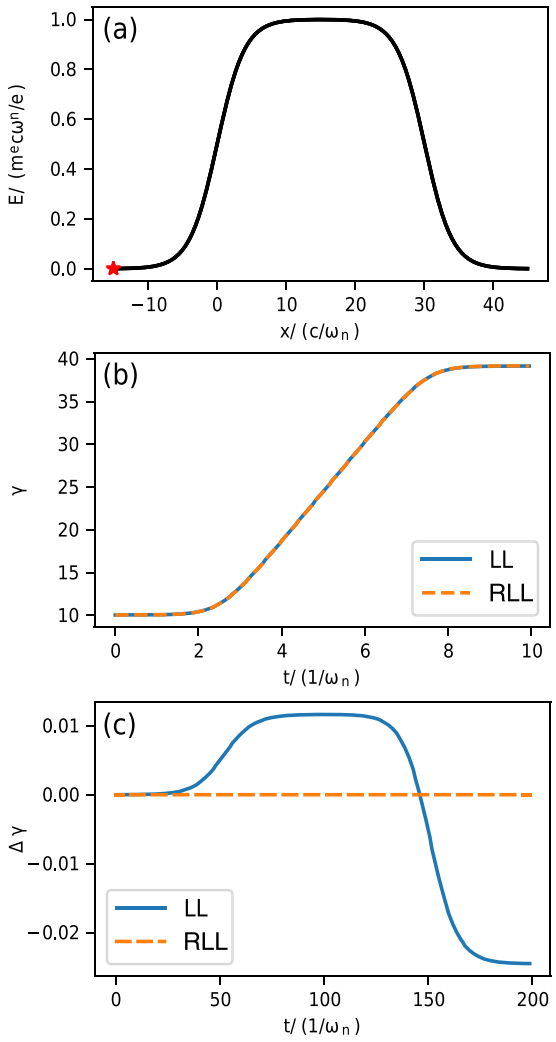

FIG. 7. (a) Spatial distribution of the electric field E_x. The red star denotes the initial location of the positron. (b) Lorentz factor γ versus time for the positron. (c) Difference of γ compared to the result without the RR, i.e., the positron follows the Lorentz equation. The solid blue line denotes the whole LL equation. The dashed orange line denotes the reduced LL equation, i.e., the derivative term is neglected.

is as follows:

$$\frac{d\boldsymbol{p}}{dt} = e(\boldsymbol{E} + \boldsymbol{v} \times \boldsymbol{B}) + \frac{2e^4}{3m^2c^4 4\pi\varepsilon_0}\left\{\gamma\frac{mc}{e}\left(\frac{d}{dt}\boldsymbol{E} + \boldsymbol{v} \times \frac{d}{dt}\boldsymbol{B}\right)\right.$$
$$+ [c\boldsymbol{E} \times \boldsymbol{B} + c\boldsymbol{B} \times (\boldsymbol{B} \times v) + \boldsymbol{E}(\beta \cdot \boldsymbol{E})]$$
$$\left. - \gamma^2\boldsymbol{\beta}[(\boldsymbol{E} + \boldsymbol{v} \times \boldsymbol{B})^2 - (\boldsymbol{E} \cdot \boldsymbol{\beta})^2]\right\}. \quad \text{(A1)}$$

To benchmark our implementation, we let a positron with $\gamma = 10$ propagate along the x axis in a static external parallel electric field with a large gradient. The electric field is given by the expression

$$\boldsymbol{E} = \frac{E_0}{2}\left(\frac{e^{x/a} - e^{-x/a}}{e^{x/a} + e^{-x/a}} + \frac{e^{(L-x)/a} - e^{-(L-x)/a}}{e^{(L-x)/a} + e^{-(L-x)/a}}\right)\boldsymbol{e}_x, \quad \text{(A2)}$$

where $E_0 = 1 \approx 0.2E_{cr}$, $a = 4c/\omega_n$, $L = 30c/\omega_n$, $E_{cr} = 1.32 \times 10^{18}$ V/m is the Schwinger limit, and $\omega_n \approx 4.78 \times 10^{21}$. The spatial distribution of the electric field E_x is shown in Fig. 7(a). The positron is initially positioned at $x = -15c/\omega_n$ (red star) and moves along the x axis with $\gamma = 10$. The parameters chosen here are the same as in Ref. [34].

In such a configuration with $\boldsymbol{E} \parallel \boldsymbol{p}$ and $\boldsymbol{B} = 0$, the LL equation reduces to

$$\frac{d\boldsymbol{p}}{dt} = e\boldsymbol{E} + \frac{1}{4\pi\varepsilon_0}\frac{2e^3}{3mc^3}\boldsymbol{v}\frac{\partial \boldsymbol{E}}{\partial x}. \quad \text{(A3)}$$

If we omit the second term of (A1), which is so-called reduced LL (RLL) equation, then the second term of (A3) is eliminated. Thus the RLL equation coincides with the Lorentz equation.

Figure 7(b) shows the evolution of the Lorentz factor of the positron obtained by the LL and RLL equations. As we can see from this figure, although the electric-field gradient here is very high, the difference between these two equations is negligible. The deviation from these two equations to the Lorentz equation is plotted in Fig. 7(c). It is obvious that the RLL equation coincides with the Lorentz equation. The LL equation, however, differs slightly from the Lorentz equation, as described by Eq. (A3). The results shown here fit well with Fig. 3 in Ref. [34]. Note that we have adopted the complete form (A1) throughout this paper.

[1] eli-laser.eu

[2] J. Zou, C. Le Blanc, D. Papadopoulos, G. Chériaux, P. Georges, G. Mennerat, F. Druon, L. Lecherbourg, A. Pellegrina, P. Ramirez *et al.*, High Power Laser Sci. Eng. **3**, e2 (2015).

[3] C. Hernandez-Gomez, S. P. Blake, O. Chekhlov, R. J. Clarke, A. M. Dunne, M. Galimberti, S. Hancock, R. Heathcote, P. Holligan, A. Lyachev, P. Matousek, I. O. Musgrave, D. Neely, P. A. Norreys, I. Ross, Y. Tang, T. B. Winstone, B. E. Wyborn, and J. Collier, J. Phys.: Conf. Ser. **244**, 032006 (2010).

[4] www.xcels.iapras.ru.

[5] R. T. Hammond, Electron. J. Theor. Phys. **7**, 221 (2010).

[6] K. Poder, M. Tamburini, G. Sarri, A. Di Piazza, S. Kuschel, C. D. Baird, K. Behm, S. Bohlen, J. M. Cole, D. J. Corvan *et al.*, Phys. Rev. X **8**, 031004 (2018).

[7] J. M. Cole, K. T. Behm, E. Gerstmayr, T. G. Blackburn, J. C. Wood, C. D. Baird, M. J. Duff, C. Harvey, A. Ilderton, A. S. Joglekar *et al.*, Phys. Rev. X **8**, 011020 (2018).

[8] A. Di Piazza, K. Z. Hatsagortsyan, and C. H. Keitel, Phys. Rev. Lett. **105**, 220403 (2010).

[9] T. G. Blackburn, C. P. Ridgers, J. G. Kirk, and A. R. Bell, Phys. Rev. Lett. **112**, 015001 (2014).

[10] H. Y. Wang, X. Q. Yan, and M. Zepf, Phys. Plasmas **22**, 093103 (2015).

[11] T. G. Blackburn, Plasma Phys. Controlled Fusion **57**, 075012 (2015).

[12] X. B. Li, B. Qiao, H. X. Chang, H. He, W. P. Yao, X. F. Shen, J. Wang, Y. Xie, C. L. Zhong, C. T. Zhou *et al.*, Phys. Rev. A **98**, 052119 (2018).

[13] N. Neitz and A. Di Piazza, Phys. Rev. Lett. **111**, 054802 (2013).

[14] M. Vranic, T. Grismayer, R. A. Fonseca, and L. O. Silva, New J. Phys. **18**, 073035 (2016).
[15] F. Niel, C. Riconda, F. Amiranoff, R. Duclous, and M. Grech, Phys. Rev. E **97**, 043209 (2018).
[16] C. Arran, J. M. Cole, E. Gerstmayr, T. G. Blackburn, S. P. Mangles, and C. P. Ridgers, Plasma Phys. Controlled Fusion **61**, 074009 (2019).
[17] C. D. Baird, C. D. Murphy, T. Blackburn, A. Ilderton, S. Mangles, M. Marklund, and C. P. Ridgers, New J. Phys. **21**, 053030 (2019).
[18] T. Blackburn, arXiv:1910.13377.
[19] Y.-F. Li, Y.-T. Zhao, K. Z. Hatsagortsyan, C. H. Keitel, and J.-X. Li, Phys. Rev. A **98**, 052120 (2018).
[20] J.-X. Li, K. Z. Hatsagortsyan, and C. H. Keitel, Phys. Rev. Lett. **113**, 044801 (2014).
[21] X. Geng, L. Ji, B. Shen, B. Feng, Z. Guo, Q. Yu, L. Zhang, and Z. Xu, Commun. Phys. **2**, 66 (2019).
[22] F. Niel, C. Riconda, F. Amiranoff, M. Lobet, J. Derouillat, F. Pérez, T. Vinci, and M. Grech, Plasma Phys. Controlled Fusion **60**, 094002 (2018).
[23] A. Macchi, Physics **11**, 13 (2018).
[24] C. N. Harvey, A. Gonoskov, M. Marklund, and E. Wallin, Phys. Rev. A **93**, 022112 (2016).
[25] J.-X. Li, Y.-Y. Chen, K. Z. Hatsagortsyan, and C. H. Keitel, Sci. Rep. **7**, 11556 (2017).
[26] G. Samarin, M. Zepf, and G. Sarri, J. Mod. Opt. **65**, 1362 (2017).
[27] C. P. Ridgers, J. G. Kirk, R. Duclous, T. G. Blackburn, C. S. Brady, K. Bennett, T. D. Arber, and A. R. Bell, J. Comput. Phys. **260**, 273 (2014).
[28] L. D. Landau, *The Classical Theory of Fields* (Elsevier, Amsterdam, 2013), Vol. 2.
[29] J. Schwinger, Proc. Natl. Acad. Sci. USA **40**, 132 (1954).
[30] V. B. Berestetskii, E. M. Lifshitz, and L. P. Pitaevskii, *Quantum Electrodynamics*, 2nd ed., Course of Theoretical Physics Vol. 4 (Butterworth-Heinemann, Oxford, 1982).
[31] *Issues in Intense-Field Quantum Electrodynamics*, edited by V. L. Ginzburg (Nova Science, Hauppauge, 1987).
[32] I. V. Sokolov, J. A. Nees, V. P. Yanovsky, N. M. Naumova, and G. A. Mourou, Phys. Rev. E **81**, 036412 (2010).
[33] V. Baier, V. Katkov, and V. Strakhovenko, Radiat. Eff. Defects Solids **122**, 527 (1991).
[34] M. Vranic, J. L. Martins, R. A. Fonseca, and L. O. Silva, Comput. Phys. Commun. **204**, 141 (2016).
[35] Y. Zhang and S. Krasheninnikov, Phys. Plasmas **26**, 010702 (2019).
[36] T. Z. Esirkepov, S. S. Bulanov, J. K. Koga, M. Kando, K. Kondo, N. N. Rosanov, G. Korn, and S. V. Bulanov, Phys. Lett. A **379**, 2044 (2015).
[37] S. Bulanov, T. Z. Esirkepov, J. Koga, S. Bulanov, Z. Gong, X. Yan, and M. Kando, J. Plasma Phys. **83**, 905830202 (2017).
[38] T. D. Arber, K. Bennett, C. S. Brady, A. Lawrence-Douglas, M. G. Ramsay, N. J. Sircombe, P. Gillies, R. G. Evans, H Schmitz, A. R. Bell, and C. P. Ridgers, Plasma Phys. Controlled Fusion **57**, 113001 (2015).
[39] C. P. Ridgers, T. G. Blackburn, D. Del Sorbo, L. E. Bradley, C. Slade-Lowther, C. D. Baird, S. P. D. Mangles, P. McKenna, M. Marklund, C. D. Murphy *et al.*, J. Plasma Phys. **83**, 715830502 (2017).
[40] J. G. Kirk, Plasma Phys. Controlled Fusion **58**, 085005 (2016).
[41] Z. Gong, R. Hu, Y. Shou, B. Qiao, C. Chen, F. Xu, X. He, and X. Yan, Matter Radiat. Extremes **1**, 308 (2016).
[42] A. Gonoskov, A. Bashinov, I. Gonoskov, C. Harvey, A. Ilderton, A. Kim, M. Marklund, G. Mourou, and A. Sergeev, Phys. Rev. Lett. **113**, 014801 (2014).
[43] G. Lehmann and K. H. Spatschek, Phys. Rev. E **85**, 056412 (2012).
[44] C. Baumann and A. Pukhov, Phys. Rev. E **94**, 063204 (2016).
[45] H. X. Chang, B. Qiao, Z. Xu, X. R. Xu, C. T. Zhou, X. Q. Yan, S. Z. Wu, M. Borghesi, M. Zepf, and X. T. He, Phys. Rev. E **92**, 053107 (2015).
[46] T. Z. Esirkepov and S. V. Bulanov, Phys. Lett. A **381**, 2559 (2017).
[47] A. M. Fedotov, N. V. Elkina, E. G. Gelfer, N. B. Narozhny, and H. Ruhl, Phys. Rev. A **90**, 053847 (2014).
[48] C. Shen and D. White, Phys. Rev. Lett. **28**, 455 (1972).
[49] R. Duclous, J. G. Kirk, and A. R. Bell, Plasma Phys. Controlled Fusion **53**, 015009 (2011).